Semi-solid alkali metal electrodes enabling high critical current densities in solid electrolyte batteries

Citation: Park, Richard J-Y, Eschler, Christopher M, Fincher, Cole D, Badel, Andres F, Guan, Pinwen et al. 2021. "Semi-solid alkali metal electrodes enabling high critical current densities in solid electrolyte batteries." Nature Energy, 6 (3).

As Published: 10.1038/S41560-021-00786-W

Publisher: Springer Science and Business Media LLC

Persistent URL: https://hdl.handle.net/1721.1/142488

Version: Author's final manuscript: final author's manuscript post peer review, without publisher's formatting or copy editing

Semi-Solid Alkali Metal Electrodes Enabling High Critical Current Densities in Solid Electrolyte Batteries

Richard J.-Y. Park[1], Christopher M. Eschler[1], Cole D. Fincher[1,2], Andres F. Badel[1], Pinwen Guan[3], Matt Pharr[2], Brian W. Sheldon[4], W. Craig Carter[1], Venkatasubramanian Viswanathan[3], Yet-Ming Chiang[1,*]

[1]Department of Materials Science & Engineering

Massachusetts Institute of Technology, Cambridge, MA 02139 USA

[2]Department of Mechanical Engineering

Texas A&M University, College Station, TX 77843 USA

[3]Department of Mechanical Engineering

Carnegie Mellon University, Pittsburgh, PA 15213 USA

[4]School of Engineering,

Brown University, Providence, RI 02019, USA

[*]Corresponding author: ychiang@mit.edu

Abstract

The need for higher energy density rechargeable batteries has generated interest in alkali metal electrodes paired with solid electrolytes. However, metal penetration and electrolyte fracture at low current densities have emerged as fundamental barriers. Here, we show that for pure metals in the Li-Na-K system, the critical current densities scale inversely to mechanical deformation resistance. Furthermore, we demonstrate two electrode architectures in which the presence of a liquid phase enables high current densities while preserving the shape retention and packaging advantages of solid electrodes. First, biphasic Na-K alloys show K^+ critical current densities (with K-β″-Al_2O_3 electrolyte) that exceed 15 mA·cm^{-2}. Second, introducing a wetting interfacial film of Na-K liquid between Li metal and $Li_{6.75}La_3Zr_{1.75}Ta_{0.25}O_{12}$ (LLZTO) solid electrolyte doubles the critical current density and permits cycling at areal capacities exceeding 3.5 mAh·cm^{-2}. These design approaches hold promise for overcoming electro-chemo-mechanical stability issues that have heretofore limited performance of solid-state metal batteries.

Introduction

Rechargeable batteries have enabled advances in portable electronics, transportation, and renewable energy storage over the past two decades. Today's electric vehicle (EV) lithium-ion batteries possess a combination of high specific energy (~150 $Wh \cdot kg^{-1}$ at pack-level) and high energy density (~250 $Wh \cdot L^{-1}$ at pack-level)[1] with cycle life that is on track to reach 5000 cycles.[2] However, future applications such as electric aviation[3] will require additional radical improvements. One promising approach is to use metallic negative electrodes, especially lithium,[4] which provides for high cell voltage and capacity (3869 $mAh \cdot g^{-1}$ and 2066 $Ah \cdot L^{-1}$ theoretical capacities).

However, use of lithium metal anodes with liquid electrolytes has met significant challenges, most importantly poor coulombic efficiency and susceptibility to short circuits due to dendrite formation at practical current densities (1–3 $mA \cdot cm^{-2}$).[5,6] An alternative approach pairs lithium metal anodes with inorganic solid electrolytes, and could result in safer as well as energy-dense batteries.[4,7-9] Inorganic solid electrolytes (SEs) such as lithium sulfides (e.g. β-Li_3PS_4) and garnet-structure oxides (e.g. $Li_7La_3Zr_2O_{12}$) have received much attention due to their high ionic conductivity[10,11] and progress towards achieving an electrochemically stable electrode-electrolyte interface.[8] However, despite expectations that the high elastic moduli of inorganic solid electrolytes (~20 GPa for sulfides[12] and ~100–200 GPa for oxides[13]) compared to lithium metal (~5 GPa) would suppress lithium dendrites,[14] a hallmark of both single crystalline[15,16] and polycrystalline[15,17–21] lithium solid electrolytes is penetration by metal filaments upon deposition at a critical current density in the range 0.1–1 $mA \cdot cm^{-2}$ (at room temperature), too low for most practical applications. Recent experiments with sodium metal electrodes have shown higher room-

temperature deposition critical current densities of 3.0 $mA \cdot cm^{-2}$ at areal capacity of ~0.5 $mAh \cdot cm^{-2}$ (with a relatively high applied pressure of 4-12 MPa),[22] and as high as 12 $mA \cdot cm^{-2}$ at areal capacity of 0.25 $mAh \cdot cm^{-2}$(applied pressure of 3.4 MPa).[23]

Here, we demonstrate a semi-solid (i.e., multiphase liquid-solid) electrode approach that takes advantage of the high critical current density of liquid metal electrodes, while having the shape retention and cell packaging advantages of solid metal electrodes. We firstly show that the pure alkali metals, lithium, sodium, and potassium, when mated with solid electrolytes that conduct each respective alkali ion, have critical current densities that scale inversely to their mechanical deformation resistance. We then demonstrate that biphasic Na-K alloys, paired with a K-β″-Al_2O_3 solid electrolyte, can be cycled between liquid-rich and solid-rich end states at critical current densities several times higher than that achievable with the solid-state alkali metals. Furthermore, the high areal capacities at which such behavior is realized suggests "self-healing" of electrodeposition-induced defects at the metal-solid electrolyte interface. Na-K alloys permit cycling at a critical current density exceeding 15 mA/cm^2 for Na-K alloy, the highest room temperature value reported to date for a metal electrode on a solid electrolyte, and sufficient to enable 3C cycling at a typical Li-ion electrode area capacity (i.e., 3 mAh/cm^2). Finally, by introducing a small amount of Na-K liquid at the interface between a lithium metal electrode and $Li_{6.75}La_3Zr_{1.75}Ta_{0.25}O_{12}$ (LLZTO) SE, we show that the critical current density is more than doubled while cycling at practical areal capacities >3 $mAh \cdot cm^{-2}$, suggesting that degradation by void formation in solid metal electrodes[24] can be mitigated with a thin metallic liquid film.

Critical Phenomena Leading to Metal Filament Penetration

The threshold conditions for the extension of a metal filament through a solid electrolyte can be described in terms of either a critical overpotential or current density. Conceptually, both are correlated with the presence of flaws in the solid electrolyte which are filled with electrodeposited metal when the applied potential produces a flux of metal ions through the solid electrolyte, **Figure 1a**. As elaborated by Porz *et al*.,[15] metal-filled defects will propagate through solid electrolytes as a result of crack-opening stresses generated by the electrodeposition of metal that are high enough to fracture the electrolyte. Lithium accumulation inside a flaw has an associated increase in volume that produces tensile loading of the flaw, resulting in crack propagation when the elastic energy release rate exceeds the fracture resistance of the electrolyte.[15] The electrical overpotential that produces this stress is the critical overpotential, and represents a thermodynamic limit dependant on properties such as the solid electrolyte fracture toughness[12,15,16] and the surface flaw size distribution. As in the Griffith-Inglis-Orowan theory of fracture,[25-27] the largest such flaw in the solid electrolyte will have the lowest critical overpotential and tend to propagate first..

However, material transport away from regions of high stress such as the metal filament tip can relieve the electrodeposition stresses; this is fundamentally the origin of the critical current density (CCD). Since current density is equivalent to atomic electrodeposition rate (assuming 100% Coulombic efficiency), at low enough deposition rates a ductile electrodeposited metal may flow away from electrodeposition sites rapidly enough to allow the crack tip stresses to remain subcritical. The CCD therefore corresponds to an electrodeposition rate *exceeding* the metal flow rate necessary to maintain a subcritical stress. Prior work with liquid sodium electrodes in high temperature sodium-sulfur batteries considered analogous mechanical models, using Poiseuille

flow of the liquid metal to relate the stress at the sodium-filled crack to the rate of metal extrusion out of the crack set by the applied current density.[28,29] For solid metals, "extrusion" from the metal-filled crack requires creep and plastic deformation. At high homologous temperatures, creep imparts an effective viscosity and so the solid metals may behave as an "incompressible work fluid". For lithium metal, the bulk deformation behavior has recently been characterized in detail,[30,31] although size effects may also come into play at the submicrometer length scales that may be most relevant in typical solid electrolytes.[30,32]

In this work, symmetric electrochemical cells of the configuration in **Figure 1b** were used to measure the CCD at room temperature in a total of 38 cells having six distinct combinations of metal electrodes and solid electrolytes, tabulated in **Supplementary Table 1**. The cells fall within three categories as depicted in **Figure 1c**: First, solid Li, Na and K electrodes paired with their respective ion-conducting solid electrolytes; second, semi-solid Na-K electrodes paired with a potassium ion conducting solid electrolyte; and third, Lithium metal solid electrolyte with a thin interfacial film of Na-K liquid, paired with LLZTO solid electrolyte.

Critical Current Densities for Li, Na and K Metal Electrodes

The pure alkali metals lithium, sodium, and potassium were electrodeposited respectively through the solid electrolytes $Li_{6.75}La_3Zr_{1.75}Ta_{0.25}O_{12}$ (LLZTO), Na-β''-alumina (NBA), and K-β''-alumina (KBA). The three metals in their solid state differ markedly in their mechanical properties, decreasing by over a factor of three in shear modulus (at 300 K) and yield stress (at 80 K) in the order lithium – sodium – potassium,[33,34] see **Supplementary Table 2**. Their liquid state viscosities when melted also increase in this order.[35, 36] Moreover, Na metal possesses a significantly lower yield stress and increased susceptibility to creep than Li metal at bulk and small scales[30,37] We

furthermore conducted microhardness testing experiments on lithium, sodium, and potassium metal to directly measure the metal's resistance to flow. The equivalent yield stress, which is taken as one-third the hardness for ductile metals,[38] decreases in the order lithium (1.74 MPa) to sodium (0.41 MPa) to potassium (0.24 MPa), see **Figure 6b**. We expect a softer metal to exhibit a higher CCD, under equivalent conditions (e.g., stack pressure).

However, the properties of the solid electrolytes also affect the CCD. We sought a set of solid electrolytes that would allow direct comparison of behavior between the three pure metal electrodes across all three working ions (Li^+, Na^+, K^+). The three solid electrolytes used, LLZTO, NBA, and KBA, were each obtained as densely sintered polycrystalline discs, **Figures 2a** and **2b**, and determined by X-ray diffraction (XRD) to be predominantly composed of the desired ion-conducting crystalline phase, see **Supplementary Table 3**. As described in *Methods* and **Supplementary Methods**, these solid electrolytes can be processed to a similar smooth surface finish (**Supplementary Figure 1**), possess similar fracture toughnesses (2-3 $MPa \cdot m^{0.5}$, **Supplementary Figure 2**), and similar ionic conductivities (1-2 mS/cm, **Supplementary Figure 3**) For each combination of metal electrode and solid electrolyte, the CCD was measured in a symmetric cell by reversibly plating the metal in both directions at stepwise increasing galvanostatic currents until the current and potential drop across the cell indicated the onset of a short circuit, **Figure 3a**. Impedance spectroscopy (IS) was then used to confirm the short circuit, **Figure 3b**. Each cell was disassembled after cycling to failure for examination. A representative example of data for each metal electrode type appears in **Figure 4a, 4b, 4c** and **Supplementary**

Figures 4–9. The features visible in these post-mortem images, alongside the specific details of the polarization curves are discussed in **Supplementary Discussion**.

The room-temperature CCDs for sodium metal and potassium metal are clearly higher than for Li metal, both reaching maximum values of ~3 mA·cm^{-2}, vs <1 mA·cm^{-2} for Li, **Figure 5a and 6a**. Each datum in **Figures 5a** and **5b** represents one cell from present experiments as listed in **Supplementary Table 1**. The vertical lines at 1 mAh·cm^{-2} and 3 mAh·cm^{-2} in Figure 5 represent respectively a minimum areal capacity for practical application, and a typical areal capacity for current Li-ion technology. The horizontal lines at 1 mA·cm^{-2} and 3 mA·cm^{-2} represent CCD values corresponding to a 1C rate capability at those areal capacities. We focused on areal capacities in the range 1–4 mAh·cm^{-2} since results at lower areal capacity may not be relevant to high energy density batteries. For example, high cycling stability has been observed in solid-state thin film batteries[39], where areal capacities are over a factor of 5 lower than in bulk batteries. Recent studies for sodium metal in contact with NBA have reported higher CCDs than we measure here, but at lower areal capacities: 3 mA·cm^{-2} at 0.5 mAh·cm^{-2},[22] and 12 mA·cm^{-2} at 0.25 mAh·cm^{-2} areal capacity.[23] We are not aware of prior results for potassium metal. The areal capacities employed here are also several times higher than in prior work using bulk lithium metal foil electrodes, as seen in **Figures 5a** and **5b,** and on an expanded scale in **Supplementary Figure 10** for results in Li/LLZO/Li cells. The highest areal capacities we tested for lithium metal (~3.8 mAh/cm^2) are nearly ten times higher than the high end of the range available in literature.

Note that results in **Figure 5a and 5b** show a variation in areal capacity even between nominally identical experiments. This is because both the CCD and areal capacity shown are true

values based on the final measured area of the metal electrodes in the disassembled cell, which exhibits some variability, rather than the areas of the current collectors or starting electrodes.

We also expect a distribution of CCDs to be observed in these experiments, in large part because the short-circuit event is correlated with the failure of a brittle solid. It is widely accepted that brittle materials exhibit a wide distribution of measured strengths (which is normally treated with Weibull statistics) due to the existence of a distribution of defect types and sizes. Fracture is inherently stochastic as it is the largest flaws in the distribution that cause failure. Similarly, it is not surprising that measured CCD values should exhibit a range of values if failure propagates from defects and inhomogeneities at the metal-solid electrolyte interface, or even below the surface. Note that the electrode area (~1 cm^2) is many orders larger than the scale of the microstructure (tens of μm^2, **Figure 2b**) ensuring that a range of flaws will be tested. We nonetheless observe a higher average CCD as well as a higher peak CCD for sodium and potassium metal compared to lithium metal. The microstructure and porosity distribution of the three solid electrolytes used here are discussed in the **Supplementary Discussion**.

Having measured the CCD as well as the equivalent yield stress of each metal from microhardness experiments, we are able to show that within the error limits of the data, there is an approximately linear relationship between the two, see **Figure 6b**. Note that this trend is observed across solid electrolytes of nearly identical ionic conductivity (~1 mS/cm) and fracture toughness (~2-3 $MPa.m^{0.5}$), and in experiments at similar plated areal capacity (1.5-3 mAh/cm^2). This result is consistent with the flow-based model discussed earlier, in which the CCD is limited by Poiseuille flow of metal out of stress concentrating flaws. These results for the three solid metals

also establish baseline behavior for comparison with the following results for semi-solid alloy electrodes.

Semi-Solid Electrodes Increase Critical Current Density

Several recent studies have focused on use of room-temperature liquid metal electrodes, obtained from deep eutectics in Na-K,[40] Na-Cs,[41] and Ga-In.[42] A limitation of fully liquid electrodes is that the corresponding electrochemical cells must be designed around containment of the low-viscosity liquid metal, as in the case of high temperature Na-S batteries where closed-ended ceramic electrolyte tubes are typically used. Such designs may be costly or impractical, especially for compact high energy battery packs where a large number of series-connected cells are needed to reach design voltage. Our approach instead is aimed at using semi-solid mixtures which include a liquid phase in which the working alkali metal is soluble. The liquid phase provides a fast transport path for the working ion as well as flow at the microscale, enabling high CCD, while the solid phase provides structural rigidity and is a source of the working ion. In the following examples, the semi-solid electrodes have the consistency of a paste and can be assembled into a free-standing cell without specialized liquid electrode containment.

In **Figure 7a**, composition A has a starting composition 0.95K-0.05Na (by mole) and becomes enriched in potassium upon charging in a K-ion cell design where the cathode supplies working K^+ and is assembled in the discharged state. Cycling to an areal capacity of 3 mAh·cm^{-2} (corresponding to an electrode thickness change of ~51.5 μm) causes a composition swing in the Na-K electrode that is indicated by the left-pointing blue arrow in **Figure 7a**. At the end of the half-cycle, the Na-K electrode composition terminates as a mixture that is mostly the K-rich solid phase α, mixed with a small amount of liquid (3.8 mol%). (This is for the starting electrode of ~

10 μL total volume and 150 μm thickness, see *Methods*). Composition B has a higher sodium starting composition of 0.90K-0.10Na (by mole) and behaves similarly except for having a higher liquid fraction throughout, terminating the half-cycle (left-pointing red arrow) with the same two phases, but ten times more Na-K liquid, 38 mol%. Additional details of electrode depletion and enrichment during cell cycling are available in the **Supplementary Discussion**. Cells using compositions A and B reached maximum CCDs as high as 8 $mA \cdot cm^{-2}$ and 20 $mA \cdot cm^{-2}$, respectively. The average CCD values (based on N=4 and N=3 cells, respectively) are ~4 times and ~6 times higher than achieved with K metal alone (**Figure 5b, Figure 6a**). The CCDs reached with composition B (mean value of 14 $mA \cdot cm^{-2}$ at areal capacities of 1.5–2 $mAh \cdot cm^{-2}$) also exceed the highest reported room temperature value for solid Na metal cells (12 $mA \cdot cm^{-2}$, measured at a much lower areal capacity of 0.25 $mAh \cdot cm^{-2}$)[23]. The results demonstrate that even a small percentage of co-existing liquid is effective in increasing the CCD of an alkali metal electrode. Examination of **Supplementary Figures 7 and 8** respectively indicates that the area specific resistance (ASR) of the 0.95K-0.05Na/KBA/0.95K-0.05Na cell and the 0.90K-0.10Na/KBA/0.90K-0.10Na cell are both on the order of ~30 Ω cm^2; the difference in CCD is not correlated with any meaningful difference in interfacial ASR.

Interfacial Liquid Film Increases Critical Current Density

Given that Li-ion technology is more well-developed than Na-ion or K-ion, we also considered semi-solid anode design possibilities in which Li is the working ion. In the Li-Na and Li-K binary systems, the equilibrium liquid fields do not extend all the way to room temperature (see phase diagrams in **Supplementary Figure 11**), so room temperature semi-solid electrodes are not

available. In contrast, the Na-K eutectic at 260.5K (**Figure 7a**) indicates at least a limiting composition (0.32Na-0.68K, by mole) where a room temperature liquid can be accessed. Thus, an electrode design in which a thin Na-K liquid film is used in conjunction with a solid lithium metal electrode was conceived, **Figure 1c** (right panel). The Li-Na-K ternary phase diagram, **Figure 7b**, was calculated in order to determine the co-existing phases and compositions present in such an electrode. The isothermal section of this ternary diagram at 300K shows a wide two-phase field (the triangle with blue lines) within which solid Li (the BCC phase) co-exists with Na-K liquid in a simple two-phase equilibrium. The blue lines are tie lines joining the co-existing solid and liquid compositions and show that the solid lithium metal phase co-exists with liquid alloy that can take on a wide range of Na/K ratios. The Na-K liquid dissolves a small amount of lithium; this solubility cannot be resolved in **Figure 7b**. The solubility has also been calculated and is shown in **Figure 7c**. The solubility of lithium is highest in Na-rich liquids and decreases by about a factor of 20 from the Na-rich to K-rich liquids that can co-exist with Li metal, but the lithium solubility in the liquid is less than 1% throughout. There are no ternary phases.

Based on this understanding, we constructed cells in which a thin layer of the Na-K eutectic liquid was placed at the interface between LLZTO and a Li metal foil electrode. This interfacial metal film may serve one or both of two functions. The first is to transport lithium from the solid lithium metal electrode to the solid electrolyte while maintaining a conformal liquid layer of negligible yield stress, thereby raising the CCD. The second is to act as an electronically conductive “liquid current collector” that can flow to fill any voids that would otherwise form in the solid lithium electrode during stripping and plating. In this role the liquid metal film may homogenize the plating current density, reducing the risk for short-circuits and enabling higher

areal capacities. One or both functions provide "self-healing" characteristics to the electrode as they mitigate the formation of interfacial defects that are exacerbated upon cycling.

We performed sessile-drop wetting experiments which showed that the Na-K eutectic alloy has a lower contact angle on LLZTO than any of the pure alkali metals (see **Supplementary Figure 12**) at temperatures where all are liquid, and lower than the contact angle of solid lithium on LLZTO.[44] This indicates that in our cell design, the Na-K eutectic liquid will wet the LLZTO in preference to the solid Li metal, thereby remaining as an interfacial film in between the LLZTO and lithium metal.

Cycling tests were conducted over a wide range of areal capacities from 0.25 to 3.7 $mAh \cdot cm^{-2}$, **Figure 5a and 5b**. Compared to the control cells using lithium metal alone, both the average and the maximum CCD values are about a factor of two higher. The average CCD increased from 0.50 $mA \cdot cm^{-2}$ (Li) to 1.21 $mA \cdot cm^{-2}$ (Li–NaK), and for the latter, several cells approached 2 $mA \cdot cm^{-2}$, **Figure 5a**. Equally important, however, the higher CCDs with the alloy approach could be accessed at areal capacities as high as 3.8 $mAh \cdot cm^{-2}$, which is nearly an order of magnitude higher than the highest values in previous literature studies for lithium metal, where areal capacities are $<0.40\ mAh \cdot cm^{-2}$ (see **Figure 5** and **Supplementary Figure 10**). The low and stable impedance of the cells using the Na-K liquid between the lithium metal and LLZTO throughout the cycling experiments suggests low chemical reactivity between the Na-K liquid and LLZTO. In our wetting experiments, there also was no evidence of reactivity between the Na-K liquid and polished LLZTO surfaces.

From these results we infer firstly that Li is transported through the Na-K liquid layer, and secondly that a thin continuous film of the Na-K liquid is retained at the LLZTO - Li metal

interface. When the lithium metal is removed from the solid electrolyte surface, the Na-K liquid, which is distinguishable from the lithium metal by its high reflectivity, remains on both the LLZTO surface and the lithium metal disc. The thickness and volumetric distribution of the interfacial NaK layer during cell cycling are discussed in the **Supplementary Discussion.**

In addition, features were observed in the electrochemical tests which support the interpretation that interfacial defects such as voids formed during lithium stripping are indeed "healed" in the presence of interfacial Na-K liquid. For the cells with purely lithium metal electrodes, attempts to cycle the cells to current densities greater than ~1.0 $mA \cdot cm^{-2}$ were unsuccessful due to an "open circuit" failure mode characterized by a large impedance rise after several galvanostatic cycles. An example of such impedance rise is seen in **Supplementary Figure 4a**, starting at the 4^{th} cycle of the Li/LLZTO/Li symmetric cell cycling at 0.5 $mA \cdot cm^{-2}$ current density with 1.5 $mAh \cdot cm^{-2}$ areal capacity (~7.5 μm lithium metal deposited per half-cycle), and continuing in subsequent cycles. This rise in impedance is consistent with interfacial void formation, and eventual delamination.[22]

This failure mode was not observed in any of the fourteen cells tested where the interfacial Na-K liquid was introduced between the Li metal foil and the solid electrolyte. An example in **Supplementary Figure 9a** shows the polarization remaining below 300 mV in the 6^{th} cycle of a cell cycling at areal capacity of 3.0 $mAh \cdot cm^{-2}$ (~15 μm lithium thickness per half-cycle) at 1.5 $mA \cdot cm^{-2}$, corresponding to ~180 μm cumulative Li thickness deposited. We attribute the greater stability at higher per-cycle and cumulative areal capacities to the *in-situ* healing of interfacial defects formed during Li metal stripping.[24] Kasemchainan *et al*.[24] found that the effects of void formation can be reduced by the application of a substantial stack pressure (e.g., 7 MPa). In our

experiments, this failure mode appears to be mitigated even at very low stack pressure (e.g., ~75 kPa, **Figure 5a**) upon introduction of the interfacial liquid film.

Conclusions

The critical current density at which metal penetration occurs through solid electrolytes leading to an electrical short circuit has been explored for metal electrodes that represent three distinct strategies towards higher performance: Lowering the yield stress of a solid metal electrode, using semi-solid electrodes consisting of co-existing solid and liquid alkali metal phases, and introducing a wetting interfacial liquid film between the electroactive metal and solid electrolyte. With increasing ductility of the pure metal, e.g., for Na and K, the CCD is 4-5 times higher than for pure Li metal. It is possible to further increase the CCD to nearly 15 $mA \cdot cm^{-2}$ by using a biphasic, or semi-solid Na-K electrode. This approach, which yields the high CCD of a liquid metal electrode without sacrificing the packaging advantages of a solid electrode, enables the highest critical current density reported to date for any alkali metal electrode at room temperature. When a thin film of interfacial Na-K liquid is introduced between the lithium metal and solid electrolyte, a factor of two increase in the CCD is accompanied by the ability to cycle to areal capacities greater than 3.5 $mAh \cdot cm^{-2}$, and at stack pressures as low as 75 kPa. For both the semi-solid electrode approach and the interfacial liquid film approach, the ability to cycle at high areal capacities without impedance rise indicates that failure modes such as interfacial void formation can be averted. These design approaches can be extended to other alloy systems. Further development of these strategies may be fruitful in the pursuit of high-energy density all-solid-state batteries.

Methods

Materials

Solid electrolytes: Polycrystalline $Li_{6.75}La_3Zr_{1.75}Ta_{0.25}O_{12}$ (LLZTO) was obtained from Toshima Manufacturing Inc, Saitama, Japan, and Na-β''-alumina (NBA), and K-β''-alumina (KBA) samples were obtained from Ionotec, Runcorn, Great Britain. All electrolytes had dimensions of ½ inch diameter and ~1 mm thickness. The crystal structure, single crystallinity, and phase purity of the electrolytes were determined via X-ray diffraction (XRD) using a PANalytical X'Pert Pro diffractometer (Malvern Panalytical Ltd, Malvern, England) (**Supplementary Table 3**).

Electrochemical Impedance Spectroscopy (IS) was performed on the solid electrolytes using sputtered Au electrodes (blocking Li, Na, and K-ions) on either side of the solid electrolyte disc using a Bio-Logic VMP-3 cell test system (Knoxville, Tennessee, USA). The Au thin film (~100 nm), which acts as the electrical contact between the ceramic electrolyte disc and the test system, was deposited onto the electrolyte via magnetron sputtering (Cressington, Watford, England). Values for ionic conductivity (and dielectric capacitance) were extrapolated from circuit fitting of resulting IS spectra (**Supplementary Figure 3**).

A Vickers micro-indenter (LECO LM248AT Microindentation hardness testing system, St. Joseph, Michigan, USA) was used to place several indents under enough applied load to produce cracks that emanate from the corners. These cracks have a semicircular crack front that extends normal to the surface into the crystal. By varying the applied load, a range of crack lengths is produced. An SEM image of an indent showing the characteristic corner cracks, appears in **Supplementary Figure 2**. Indentation loads of 19.6 N, 9.81 N, and 4.91 N were used to determine the fracture toughness in this study. The crack lengths were measured via optical microscopy.

The corresponding hardness (determined from the square-pyramid indent size) and fracture toughness (determined from the crack length) of the solid electrolytes are summarized in **Supplementary Figure 2**.

Two independent methods (Anstis *et al.*[43] and Evans *et al.*[44]) for obtaining the fracture toughness from indentation data were used. The Anstis method requires a value for Young's modulus of the indented material,[43] whilst the Evans method is modulus independent.[44] Results are shown in **Supplementary Figure 2**.

The ground electrolyte discs (1-mm thickness) received from the vendor were polished using an EcoMet™ 250 Pro Grinder Polisher (Buehler, Lake Bluff, Illinois, USA). To obtain finely polished faces, the samples were then sequentially polished using aqueous diamond suspensions of 9 μm and 1 μm particle size, for 25 min and 10 min, respectively. The samples were then ultrasonically cleaned in DI water to remove polishing debris.

Thermal etching of the polished solid electrolytes (1 hour at 500°C, 1000°C, 1000°C for LLZTO, NBA, KBA respectively) reveal the grain size to range from 5 to 10 μm for all three solid electrolytes. SEM imaging of the samples was conducted using a JEOL 6610 LV SEM (JEOL USA Inc, Peabody, MA, USA) operating at 15 kV accelerating potential and 215 pA current. All samples were prepared in an argon-filled glove box (oxygen and water levels below 0.1 ppm).

Stylus profilometry was conducted using a Bruker DXT Stylus Profilometer (Bruker, Billerica, Massachusetts, USA) to quantify the roughness of the polished samples. Representative data is shown in **Supplementary Figure 1**.

Alkali metals: Lithium foil (750 mm) was sourced from Alfa Aesar, Haverhill, Massachusetts, USA. Cubes of sodium and potassium immersed in mineral oil were sourced from Sigma Aldrich,

St. Louis, MO, US. The lithium metal was prepared for cell assembly by cold rolling to the desired thickness between polyethylene sheets and punching a disc of desired diameter. The sodium and potassium metal electrodes were melted in the glove box and applied as a liquid to the surfaces of solid electrolyte discs held at room temperature, whereupon the liquid metals quickly froze. The Na-K alloys were prepared by melting the pure sodium and potassium, pipetting by volume into a glass vial in desired ratio of metals, homogenizing by heating into a single-phase liquid regime, and cooling.

Microhardness testing: Lithium metal rods (Millipore Sigma, item 265969), sodium metal bars (Alfa Aesar, item L13285), and potassium metal lumps (Alfa Aesar, item 13267) were sectioned using a razor blade into pieces approximately 1 inch diameter by 3/4 inch thick within an argon-filled glovebox. The bottom surface of each sample was rigidly fixed to a ½ inch stainless steel plate using cyanoacrylate adhesive. This assembly was then placed between two well-oiled borosilicate glass plates (1/4-inch-thick, lubricated with white mineral oil) inside a hydraulic crimper. Subsequently, the pieces were pressed until flat and covered with a thick (≈3 mm) layer of petroleum jelly. The resulting samples were removed from the glovebox and microhardness tests were conducted through the petroleum jelly using a phase II + model 900-390A microhardness tester. The loading to maximum force (0.245 N) occurred over 15 s. Hardness measurements were calculated as the applied load (0.245 N) divided by the projected contact area.

Electrochemical cell assembly

Prior to assembly, the polished solid electrolyte discs were heat treated in an argon-filled glove box at oxygen and water content below 0.1 ppm and 0.1 ppm, respectively), which has been shown to remove surface impurity layers on the electrolyte and reduce the interfacial impedance.[45] Polished LLZTO discs were heat treated in the glove box at 500°C for 3 hours to remove $LiCO_3$ and LiOH.[45] The NBA and KBA pellets were subjected to heat treatment at 1000°C for 1 hour in the glove box in order to remove possible chemisorbed moisture.

Lithium metal symmetric cells were assembled by placing a disc of flat lithium foil (0.375" diameter, 0.25 mm thickness, 50 $mAh \cdot cm^{-2}$, ~20 μL lithium) between the LLZTO solid electrolyte with a stainless-steel cylinder acting as the current collector on either side. Before electrochemical cycling, the lithium cells were heated to 170°C for 3h at an applied stack pressure of 1.5 MPa (calibrated independently with a compression force gauge), which reduced the interfacial impedance of the cell. The area-specific interfacial impedance of the cells was measured to be on the order of 25–35 $\Omega \cdot cm^{-2}$. For cells cycled under even lower pressure (~75 kPa), the springs in the fixture were compressed to a few percent strain based on visual inspection.

Sodium metal, potassium metal, and sodium-potassium alloy cells were assembled by pipetting a 10-μL drop of molten Na, K, or pre-mixed Na-K alloy onto their respective solid electrolytes and flattening the droplet with the steel current collector (0.281" diameter) under an applied stack pressure of 1.5 MPa. No pre-cycling heat treatment was necessary to produce a low impedance cell for testing. The capacity of the electrode and its composition change during cycling was computed on the basis of the starting electrode volume and the areal capacity reached during cycling, assuming a linear rule of mixtures for the densities of the Na-K alloys.

Lithium metal cells incorporating the eutectic Na-K alloy layer were assembled in a similar manner to those of the plain lithium cells by adding ~5 μL of eutectic Na-K alloy (68 mol% K) to one face of the punched lithium disc. The side of the lithium disc with the added Na-K alloy was placed in contact with the LLZTO solid electrolyte disc. For some of the cells in which a lithium metal electrode was used with an interfacial layer of Na-K eutectic liquid, the stack pressure was reduced to a low value of ~75 kPa.

Electrochemical Cycling

Galvanostatic experiments were conducted on the cells at 22°C using a Bio-Logic VMP-3 cell test system. Li/LLZTO/Li cells were subjected to galvanostatic cycling at nominal current densities (i.e., based on initial electrode areas) from 0.125 to 3 $mA \cdot cm^{-2}$ using 0.125 $mA \cdot cm^{-2}$ increments, at areal capacities of 1.5 $mAh \cdot cm^{-2}$ per cycle (7.5 μm lithium plating thickness). Na/NBA/Na, K/KBA/K, 0.95K-0.05Na/KBA/0.95K-0.05Na, and 0.90K-0.10Na/KBA/0.90K-0.10Na cells were subjected to galvanostatic cycling at current densities from 0.5 to 40 $mA \cdot cm^{-2}$ using 0.5 $mA \cdot cm^{-2}$ increments at nominal areal capacities of 3 $mAh \cdot cm^{-2}$ per cycle (27.4 and 51.5 μm thickness for Na and K, respectively). NaK(e)–Li/LLZTO/ NaK(e)–Li cells were subjected to galvanostatic cycling at nominal current densities from 0.25 to 3 $mA \cdot cm^{-2}$ using 0.25 $mA \cdot cm^{-2}$ increments at nominal areal capacities of 0.25, 1.5, or 3 $mAh \cdot cm^{-2}$ per cycle (1.25, 7.5, 15 μm lithium plating thickness respectively). This was done to investigate the areal capacity dependence of CCD and to compare present results with literature.

IS spectra were collected at the start of testing and at set intervals thereafter (after each galvanostatic cycle for Li/LLZTO/Li and NaK(e)–Li/LLZTO/ NaK(e)–Li cells, and after every four cycles for Na/NBA/Na, K/KBA/K, 0.95K-0.05Na/KBA/0.95K-0.05Na, and 0.90K-0.10Na/KBA/0.90K-0.10Na cells). Throughout electrochemical testing, cells remained in an argon-filled glove box with oxygen and water content below 0.1 ppm and 0.1 ppm, respectively.

We also attempted electrochemical cycling of Na^+ from Na-K through NBA. However, we observed that NBA disintegrates immediately in the presence of K and Na-K. This finding is consistent with the work of Baclig *et al*.[40], who demonstrated that NBA is chemically unstable to K metal.

Post-mortem characterization

Upon completion of electrochemical cycling, *ex-situ* microscopy was conducted on disassembled cells using a Leica DMS300 (Leica Camera, Wetzlar, Germany) digital microscope.

Phase Diagrams

The binary phase diagrams for the lithium-sodium, lithium-potassium and sodium-potassium systems and the ternary isothermal section of lithium-sodium-potassium were calculated using Thermo-Calc software based on the thermodynamic model constructed by the CALculation of PHAse Diagram (CALPHAD) modeling approach, where thermochemical data and phase equilibrium information are used to evaluate the optimal set of parameters describing the Gibbs energy of each individual phase in a thermodynamic system.[46] The gas phase is described by an ideal substitutional model, with the Gibbs energies of all the constituents taken from the Scientific

Group Thermodata Europe (SGTE) database.[47] The molar Gibbs energy of liquid phase and the three solid solution phases (FCC, BCC, HCP) consisting of n components are described by:

$$G_m^{\varphi} = \sum_{i=1}^{n} x_{A_i}^{\varphi} G_{A_i}^{\varphi} + RT \sum_{i=1}^{n} x_{A_i}^{\varphi} ln x_{A_i}^{\varphi} + \Delta G^{\varphi} \quad (1)$$

here φ represents a solution phase including elements $\{A_i | 1 \le i \le n, i \in N\}$, $x_{A_i}^{\varphi}$ the molar fraction of A_i in φ, $G_{A_i}^{\varphi}$ the molar Gibbs energy of pure A_i in the structure of φ, R the gas constant, T the temperature, and the excess Gibbs energy which is expanded as (up to ternary interactions)

$$\Delta G^{\varphi} = \sum_{i<j} x_{A_i}^{\varphi} x_{A_j}^{\varphi} I_{A_i,A_j} + \sum_{i<j<k} x_{A_i}^{\varphi} x_{A_j}^{\varphi} x_{A_k}^{\varphi} I_{A_i,A_j,A_k} \quad (2)$$

where the binary interaction I_{A_i,A_j} can be expressed in the Redlich-Kister polynomial[48]:

$$I_{A_i,A_j} = \sum_{k=0} kL_{A_i,A_j} (x_{A_i}^{\varphi} - x_{A_j}^{\varphi})^k \quad (3)$$

where the coefficient $kL_{A_i,A_j} = kX_{A_i,A_j} + kY_{A_i,A_j} * T$ describes the non-ideal interaction between A_i and A_j, with kX_{A_i,A_j} and kY_{A_i,A_j} as model parameters. The ternary interaction I_{A_i,A_j,A_k} can be written as:[49]

$$I_{A_i,A_j,A_k} = \nu_{A_i} A_i L_{A_i,A_j,A_k} + \nu_{A_j} A_j L_{A_i,A_j,A_k} + \nu_{A_k} A_k L_{A_i,A_j,A_k} \quad (4)$$

where $A_i L_{A_i,A_j,A_k}$, $A_j L_{A_i,A_j,A_k}$ and $A_k L_{A_i,A_j,A_k}$ are model parameters, and the following definitions are used:

$$\nu_{A_i} = x_{A_i}^{\varphi} + \frac{1 - x_{A_i}^{\varphi} - x_{A_j}^{\varphi} - x_{A_k}^{\varphi}}{3} \quad (5)$$

$$\nu_{A_j} = x_{A_j}^{\varphi} + \frac{1 - x_{A_i}^{\varphi} - x_{A_j}^{\varphi} - x_{A_k}^{\varphi}}{3} \quad (6)$$

$$\nu_{A_k} = x_{A_k}^{\varphi} + \frac{1 - x_{A_i}^{\varphi} - x_{A_j}^{\varphi} - x_{A_k}^{\varphi}}{3} \quad (7)$$

In the present work, the Gibbs energies of pure elements are taken from the SGTE database,[47] and the interaction parameters of the solution phases, as well as the Gibbs energy of the only stable intermetallic compound Na_2K, is adopted from the work by Zhang.[50]

Microstructural Simulation

The microstructures inset into **Figure 6a** were computed with a time-cone method algorithm[51]. All nuclei were placed at time = 0 with locations obtained from a uniform random distribution, but with a minimum separation between each nucleus. Each nucleus was given a growth-speed chosen from a random distribution from 0.6 to 1.5. The areal density of nuclei and the time-slice of the cones determine the final phase-fractions and determined by pixel counting. The time slice for the phase fractions .51 and .10 were obtained by a secant-search algorithm.

Data Availability

All relevant data are included in the paper and its **Supplementary Information**.

References

[1] Howell, D., Cunningham, B. Duong, T. & Faguy, P. Overview of DOE Vehicle Technologies Office Advanced Battery R&D Program, (2016).

[2] Harlow, J. E. *et al*. "A Wide Range of Testing Results on an Excellent Lithium-Ion Cell Chemistry to be used as Benchmarks for New Battery Technologies", *J. Electrochem. Soc.*, **166**, A3031–A3044, (2019).

[3] Bills, A., Sripad, S., Fredericks, W.L., Singh, M. & Viswanathan, V. "Performance Metrics Required of Next-Generation Batteries to Electrify Commercial Aircraft", *ACS Energy Lett.*, **5**, 663–668 (2020).

[4] Albertus, P., Babinec, S., Litzelman, S. & Newman, A. "Status and challenges in enabling the lithium metal electrode for high-energy and low-cost rechargeable batteries", *Nat. Energy*, **3**, 16–21 (2018).

[5] Aurbach, D., Zinigrad, E., Cohen, Y. & Teller, H. "A short review of failure mechanisms of lithium metal and lithiated graphite anodes in liquid electrolyte solutions", *Solid State Ionics*, **148**, 405–416 (2002).

[6] Liu, Z. *et al*. "Interfacial study on solid electrolyte interphase at Li metal anode: implication for Li dendrite growth", *J. Electrochem. Soc.*, **163**, A592–A598 (2016).

[7] Manthiram, A., Yu, X. & Wang, S. "Lithium battery chemistries enabled by solid-state electrolytes", *Nat. Rev. Mater.*, **2**, 16103 (2017).

[8] Kerman, K., Luntz, A., Viswanathan, V., Chiang, Y.-M. & Chen, Z. "Practical challenges

hindering the development of solid state Li ion batteries", *J. Electrochem. Soc.*, **164**, A1731–A1744 (2017).

[9] Janek, J. & Zeier, W.G. "A solid future for battery development", *Nat. Energy*, **1**, 16141 (2016).

[10] Thangadurai, V., Narayanan, S. & Pinzaru, D. "Garnet-type solid-state fast Li ion conductors for Li batteries: critical review", *Chem. Soc. Rev.*, **43**, 4714–4727 (2014).

[11] Liu, D. *et al*. "Recent progress in sulfide-based solid electrolytes for Li-ion batteries", *Mater. Sci. Eng. B.*, **213**, 169–176 (2016).

[12] McGrogan, F. *et al*., "Compliant Yet Brittle Mechanical Behavior of Li_2S–P_2S_5 Lithium-Ion-Conducting Solid Electrolyte", *Adv. Energy Mater.*, **7**, 1602011 (2017).

[13] Wolfenstine, J. *et al*. "A preliminary investigation of fracture toughness of $Li_7La_3Zr_2O_{12}$ and its comparison to other solid Li-ion conductors", *Mater. Lett.*, **96**, 117–120 (2013).

[14] Monroe, C. & Newman, J. "The Impact of Elastic Deformation on Deposition Kinetics at Lithium/Polymer Interfaces", *J. Electrochem. Soc.*, **152**, A396–A404 (2005).

[15] Porz, L. *et al*. "Mechanism of Lithium Metal Penetration through Inorganic Solid Electrolytes", *Adv. Energy Mater.*, **7**, 1701003 (2017).

[16] Swamy, T. *et al*., "Lithium metal penetration induced by electrodeposition through solid electrolytes: Example in single-crystal $Li_6La_3ZrTaO_{12}$ garnet." *J. Electrochem. Soc.* **165**, A3648–A3655 (2018).

[17] Aguesse, F. *et al*. "Investigating the Dendritic Growth During Full Cell Cycling of Garnet

Electrolyte in Direct Contact With Li Metal", *ACS Appl. Mater. Interfaces*, **9**, 3808–3816 (2017).

[18] Sharafi, A., Meyer, H.M., Nanda, J., Wolfenstine, J. & Sakamoto, J. "Characterizing the Li-$Li_7La_3Zr_2O_{12}$ interface stability and kinetics as a function of temperature and current density", *J. Power Sources*, **302**, 135–139 (2016).

[19] Ren, Y.Y., Shen, Y., Lin, Y.H. & Nan, C.W. "Direct observation of lithium dendrites inside garnet-type lithium-ion solid electrolyte", *Electrochem. Commun.*, **57**, 27–30 (2015).

[20] Nagao, M. *et al*. "In situ SEM study of a lithium deposition and dissolution mechanism in a bulk-type solid-state cell with a Li_2S–P_2S_5 solid electrolyte", *Phys. Chem. Chem. Phys.*, **15**, 18600–18606 (2013).

[21] Taylor, N.J. *et al*. "Demonstration of high current densities and extended cycling in the garnet $Li_7La_3Zr_2O_{12}$ solid electrolyte", *J. Power Sources*, **396**, 314–318 (2018).

[22] Jolly, D.S. *et al*. "Sodium/Na β″ Alumina Interface: Effect of Pressure on Voids", *ACS Appl. Mater. Interfaces*, **12**, 678-685 (2020).

[23] Bay, M.-C. *et al*. "Sodium Plating from Na-β″-Alumina Ceramics at Room Temperature, Paving the Way for Fast-Charging All-Solid-State Batteries", *Adv. Energy Mater.*, **10**, 1902899 (2019).

[24] Kasemchainan, J. *et al*. "Critical stripping current leads to dendrite formation on plating in lithium anode solid electrolyte cells", *Nat. Mater.*, **18**, 1105–1111 (2019).

[25] Griffith, A.A. "The phenomena of rupture and flow in solids", *Phil. Trans. Roy. Soc.*, **221A**,

163–198 (1920), “The theory of rupture”, *Proc. Int. Congr. Appl. Mech.*, 56–63 (1924).

[26] Inglis, C.E. “Stresses in a plate due to the presence of cracks and sharp notches”, *Trans. Roy. Inst. Naval Architects,* **55**, 219–241 (1913).

[27] Orowan, E. “Fracture and strength of solids”, *Rep. Prog. Phys.,* **12**, 185–232 (1949).

[28] Virkar, A.V. & Viswanathan, L. “Sodium Penetration in Rapid Ion Conductors”, *J. Am. Ceram. Soc.*, 62, 528–529 (1979).

[29] Virkar, A.V. “On some aspects of breakdown of β″-alumina solid electrolyte”, *J. Mater. Sci.*, 16, 1142–1150 (1981).

[30] Fincher, C.D., Ojeda, D., Zhang, Y., Pharr, G.M. & Pharr, M. “Mechanical properties of metallic lithium: from nano to bulk scales”, *Acta Mater.*, **186**, 215–222 (2019).

[31] LePage, W.S. *et al*. “Lithium mechanics: Roles of strain rate and temperature and implications for lithium metal batteries”, *J. Electrochem. Soc.*, **166**, A89–A97 (2019).

[32] Xu, C., Ahmad, Z., Aryanfar, A., Viswanathan, V. & J. R. Greer. “Enhanced strength and temperature dependence of mechanical properties of Li at small scales and its implications for Li metal anodes”, *Proc. Natl. Acad. Sci. USA*, 114, 57–61 (2017).

[33] Vaks, V.G., Kravchuk, S.P., Zarochentsev, E.V & Safronov, V.P. “Temperature dependence of the elastic constants in alkali metals”, *J. Phys. F Met. Phys.*, **8**, 725–742 (1978).

[34] Hull, D. & Rosenberg, H.M. “The deformation of lithium, sodium and potassium at low temperatures: Tensile and resistivity experiments”, *Philos. Mag.*, **4**, 303–315 (1959).

[35] Andrade, E.N.d.-C. & Dobbs, E.R. "The viscosities of liquid lithium, rubidium and caesium", *Proc. R. Soc. Lond. A.,* **211**, 12–30 (1952)

[36] Grosse, A.V., "Viscosities of liquid sodium and potassium, from their melting points to their critical points", *Science*, **147**, 1438-1411 (1965).

[37] Fincher, C.D., Zhang, Y., Pharr, G.M. & Pharr, M. "Elastic and Plastic Characteristics of Sodium Metal", *ACS Appl. Energy Mater.,* **3**, 1759–1767 (2020).

[38] Tabor, D. "The Hardness of Metals", Oxford University Press, (2000).

[39] Bates, J.B., Dudney, N.J., Neudecker, B., Ueda, A. & Evans, C.D. "Thin-film lithium and lithium-ion batteries", *Solid State Ion.,* **135**, 33–45 (2000).

[40] Baclig, A.C. *et al*. "High-Voltage, Room-Temperature Liquid Metal Flow Battery Enabled by Na-K|K- β″-Alumina Stability", *Joule,* **2**, 1287–1296 (2018).

[41] Liu, C., Shamie, J.S., Shaw, L.L & Sprenkle, V.L. "An Ambient Temperature Molten Sodium–Vanadium Battery with Aqueous Flowing Catholyte", *ACS Appl. Mater. Interfaces*, **8**, 1545–1552 (2015).

[42] Guo, X. *et al*. "A Self-Healing Room-Temperature Liquid-Metal Anode for Alkali-Ion Batteries", *Adv. Funct. Mater.,* **28**, 1804649 (2018).

[43] Anstis, G.R., Chantikul, P., Lawn, B.R. & Marshall, D.B. "A Critical Evaluation of Indentation Techniques for Measuring Fracture Toughness: I, Direct Crack Measurements", *J. Am. Ceram. Soc.,* **64**, 533–538 (1981).

[44] Evans, A.G. & Charles, E.A. “Fracture Toughness Determinations by Indentation”, *J. Am. Ceram. Soc.*, **59**, 371–372 (1976).

[45] Sharafi, A. *et al*. “Surface Chemistry Mechanism of Ultra-Low Interfacial Resistance in the Solid-State Electrolyte $Li_7La_3Zr_2O_{12}$”, *Chem. Mater.*, **29**, 7961–7968 (2017).

[46] Kaufman, L. “The Lattice Stability of Metals—I. Titanium and Zirconium”, *Acta Metall.*, **7**, 575–587 (1959).

[47] Dinsdale, A.T. “SGTE Data for Pure Elements”, *Calphad*, **15**, 317–425 (1991).

[48] Redlich, O. & Kister, S.T. “Algebraic Representation of Thermodynamic Properties and the Classification of Solutions”, *Ind. Eng. Chem.*, **20**, 345–348 (1948).

[49] Lukas, H., Fries, S.G. & Sundman. B. “Computational Thermodynamics: The CALPHAD Method.” Cambridge University Press (2007).

[50] Zhang, S.J. “Thermodynamic Investigation of the Effect of Alkali Metal Impurities on the Processing of Al and Mg Alloys”, Ph.D thesis, Pennsylvania State University (2006).

[51] Balluffi, R., Allen, S.M. & Carter, W.C. “Kinetics of Materials”, Wiley (2005)

Acknowledgements

The authors acknowledge support from the US Department of Energy, Office of Basic Energy Science, through award number DE-SC0002633 (J. Vetrano, Program Manager). This work made use of the MRL MRSEC Shared Experimental Facilities at MIT, supported by the National Science Foundation under award number DMR-1419807. We also acknowledge use of the MIT Nanomechanical Technology Laboratory (A. Schwartzman, Manager). We thank Tushar Swamy for helpful discussions, and Natalia Katorova and Polina Morozova for assistance with alkali metal handling procedures. We acknowledge financial support from the MIT-Skoltech Next Generation Program, award #2016-1, for the portion of the work related to potassium metal. CDF. acknowledges the support of the National Science Foundation Graduate Research Fellowship under grant No. 1746932. MP acknowledges the support of the National Science Foundation under award number DMR-1944674.

Author Contributions

R.J.-Y.P. and Y.-M.C designed the study. R.J.-Y.P. prepared, measured, and analyzed results from the electrochemical cells. C.M.E. measured the alkali metal wetting angles. C.D.F. measured the alkali metal mechanical properties. A.F.B. performed the image analysis of disassembled cells. P.G. calculated the Li-Na-K ternary phase diagram. All authors contributed to writing the manuscript.

Competing Interests

Massachusetts Institute of Technology has filed for patents on subject matter related to this manuscript in which R.J.-Y.P., Y.-M.C., P.G., and V.V. are listed inventors.

Additional Information

Supplementary information is available in the online version of the paper.

Correspondence and requests for materials should be addressed to Y.-M.C. (ychiang@mit.edu).

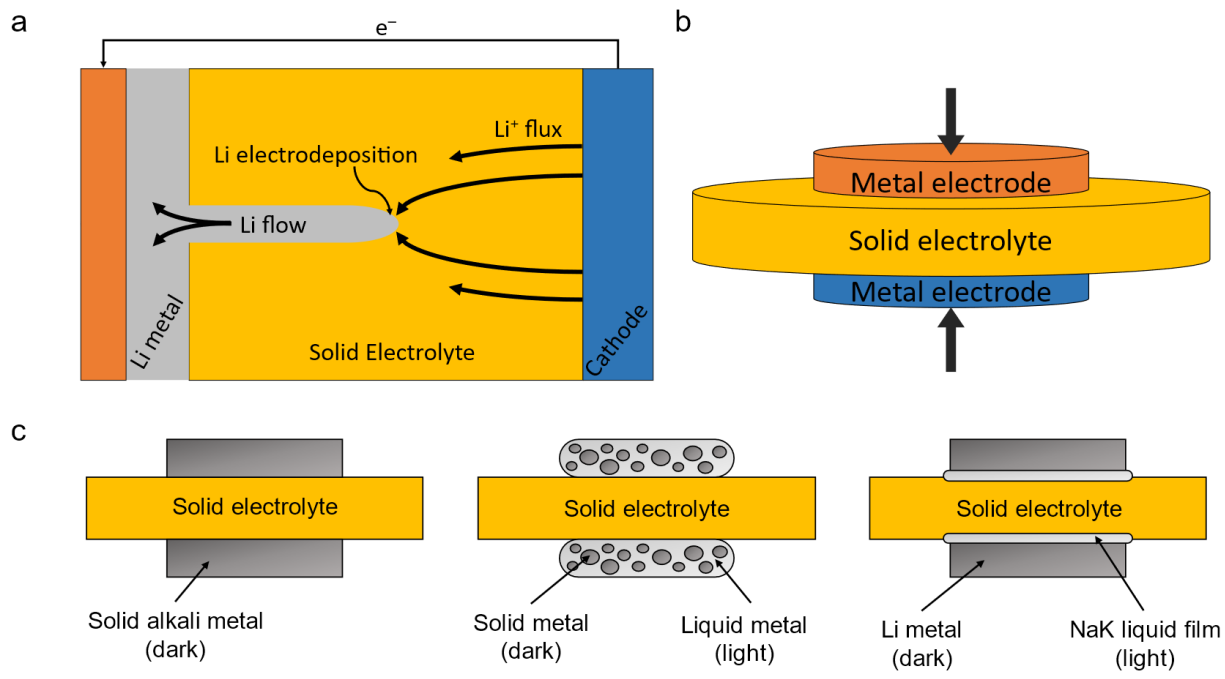

Figure 1. Overview of electrochemical cells studied. a) Lithium flux through solid electrolyte results in electrodeposition at the tip of metal-filled flaws, which readily exceed the critical overpotential for fracture[15] unless there is metal flow to relieve stress. Critical current density (CCD) is reached when electrodeposition rate exceeds metal flow rate. b) Schematic of symmetric cell configuration for CCD measurements. c) Graphical schematic summarizing the three families (all-solid-state, semi-solid, solid with interfacial liquid) of electrode materials investigated in this study.

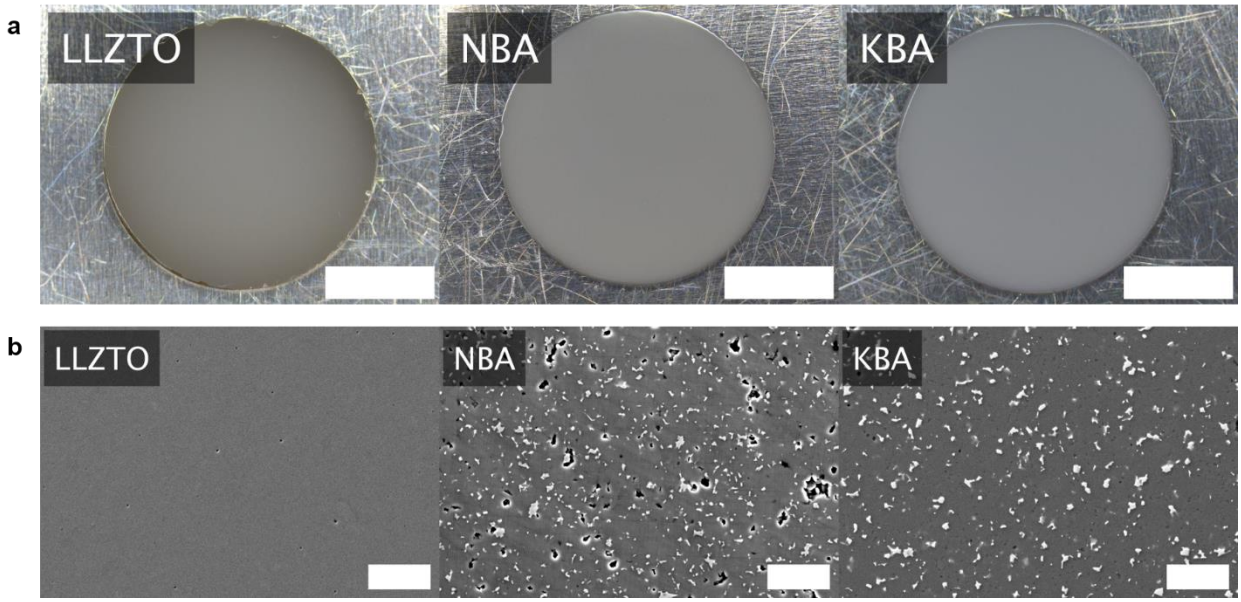

Figure 2. Surface finish and microstructure of solid electrolytes studied. a) and b) Polished discs and secondary electron images of (left to right) Li^+, Na^+ and K^+–conducting solid electrolytes. Scale bars on the digital microscopy images correspond to 5 mm. Scale bars on the electron micrographs correspond to 20 μm.

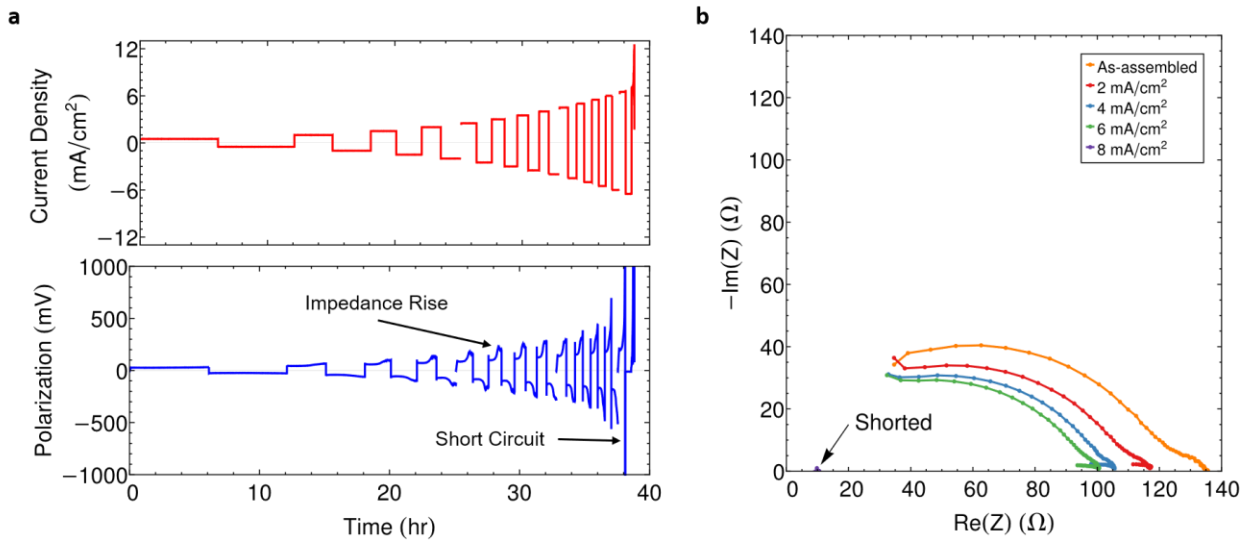

Figure 3. Critical current density for metal penetration of solid electrolytes. a) Typical current density vs time sequence and corresponding potential profile, here for a K/KBA/K symmetric cell reversibly plating 3 mAh·cm^{-2} of potassium metal. The onset of cell failure, which serves as the measurement of the CCD, is indicated by the arrow. The impedance rise is discussed in later sections of the paper. The onset of an electrical short circuit is detected as a voltage drop across the cell, here indicated by the arrow. b) Nyquist plot for the same cell. The curves connecting the individual data points act as guides for the eye. The separate-colored curves correspond to impedance spectra taken after cycling the cell at that particular current density. The presence of the capacitive arcs indicates the absence of a short circuit. A short circuit is confirmed by the collapse of the spectrum to a point, as indicated by the arrow.

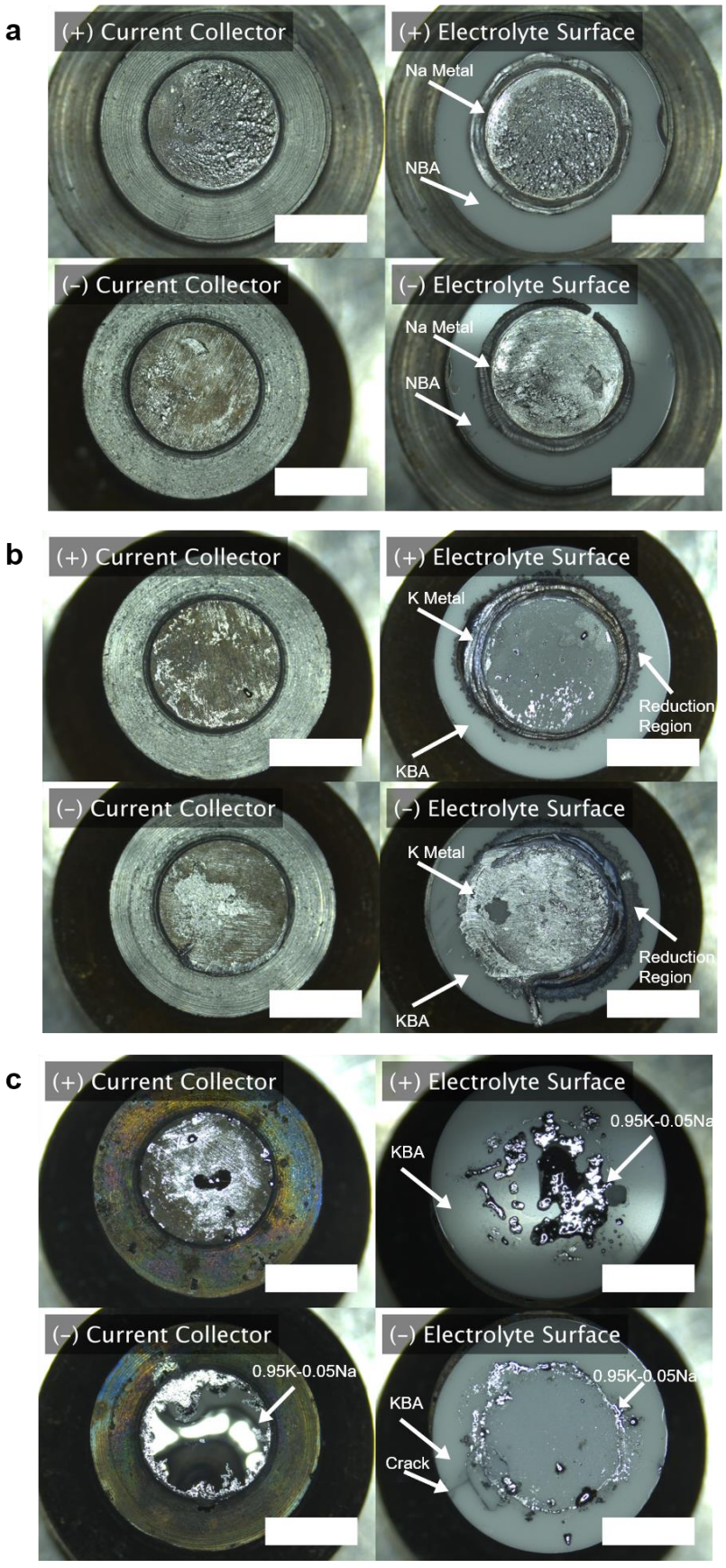
a
(+) Current Collector
(+) Electrolyte Surface
Na Metal
NBA
(-) Current Collector
(-) Electrolyte Surface
Na Metal
NBA
b
(+) Current Collector
(+) Electrolyte Surface
K Metal
Reduction Region
KBA
(-) Current Collector
(-) Electrolyte Surface
K Metal
Reduction Region
KBA
c
(+) Current Collector
(+) Electrolyte Surface
0.95K-0.05Na
KBA
(-) Current Collector
0.95K-0.05Na
(-) Electrolyte Surface
0.95K-0.05Na
KBA
Crack

Figure 4. Surfaces of positive and negative current collectors and solid electrolyte after cycling of symmetric metal-solid electrolyte cells to short-circuit failure. a) Na-metal electrodes. b) K-metal electrodes. c) 0.95K-0.05Na (by mole) semi-solid electrode. Arrow points to the probable location of the metal-filled crack(s) causing the short circuit. Scale bar is 5 mm throughout.

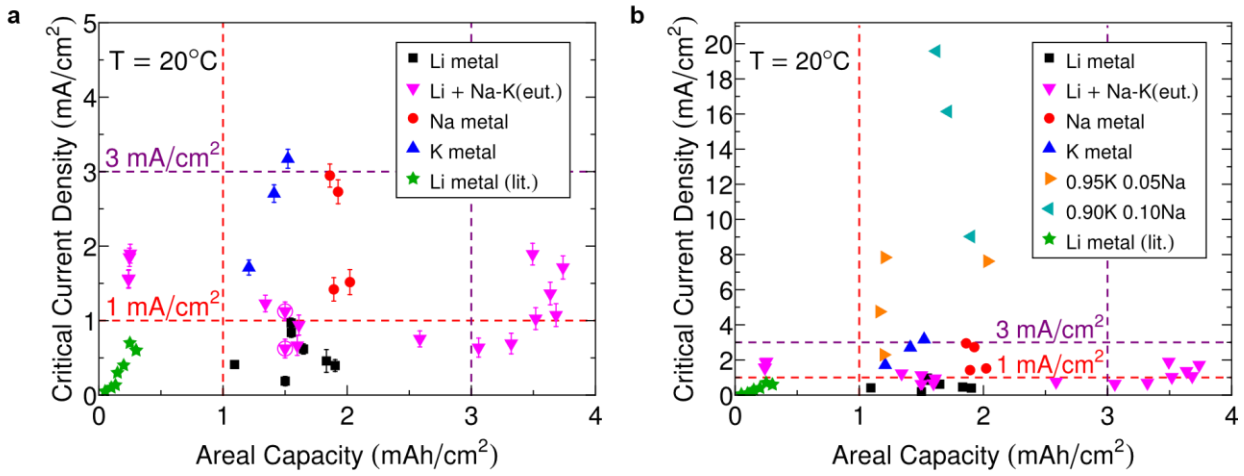

Figure 5. Critical current density (CCD) vs areal capacity for single-phase solid metals and semi-solid alloy mixtures. Each datum represents an independent cell measurement. The total span of the error bars in a) and b) represents the variation in CCD for a single increment by which the current density was stepped in the galvanostatic protocol. a) CCD for single-phase solid Li, Na, and K metal in symmetric cells using the solid electrolytes LLZTO, NBA, and KBA, and a 0.68K-0.32Na (by mole) eutectic liquid at the interface between Li metal foil and LLZTO. All experiments were conducted under nominal stack pressure of ~1.5 MPa except for circled points, which are from experiments conducted at ~75 kPa. b) CCD for all metal electrodes measured including 0.95K-0.05Na (by mole) and 0.90K-0.10 (by mole) Na semi-solid alloys.

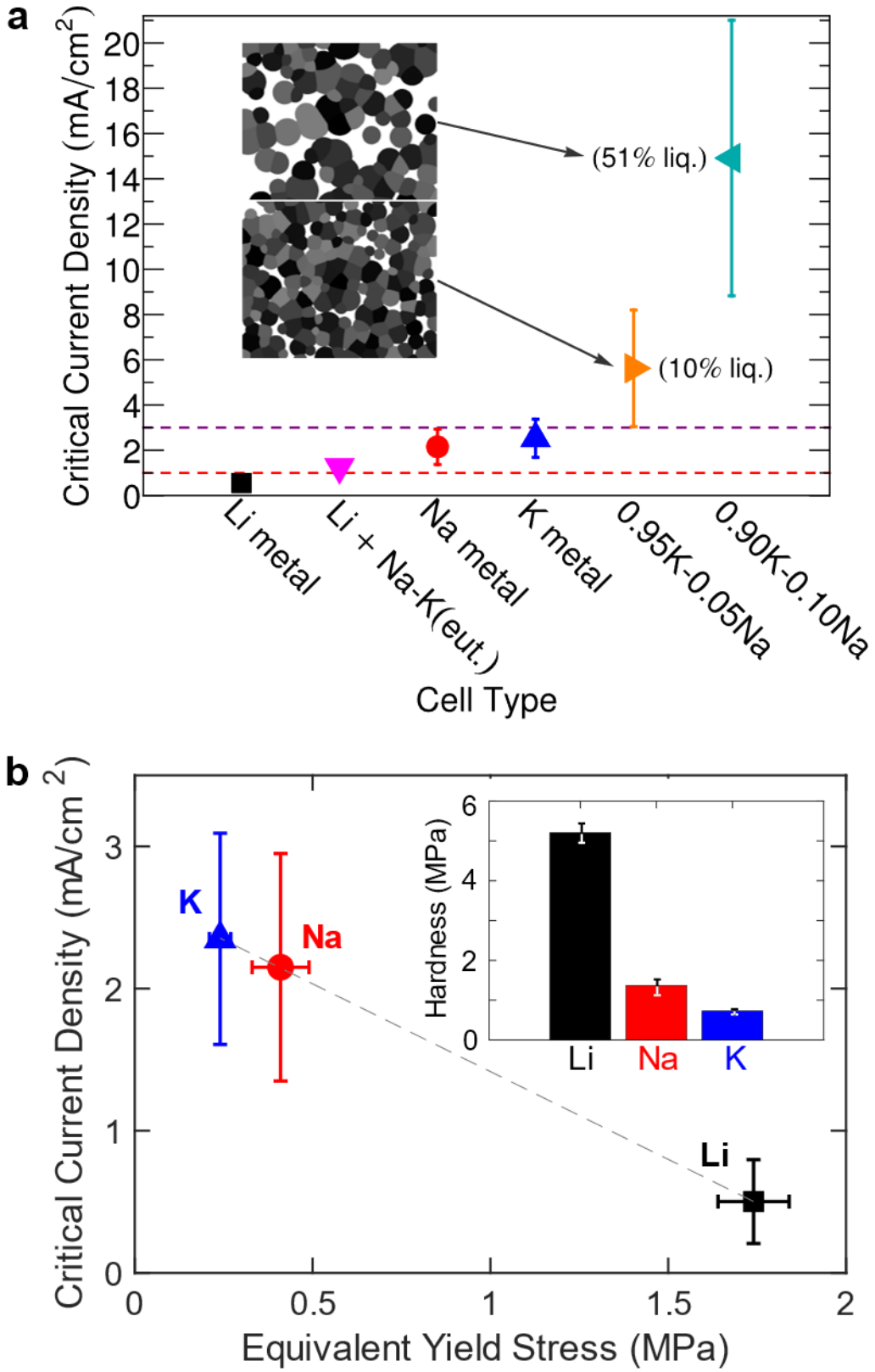
a
Critical Current Density (mA/cm^2)
20
18
16
14
12
10
8
6
4
2
0
(51% liq.)
(10% liq.)
Li metal
Li + Na-K(eut.)
Na metal
K metal
0.95K-0.05Na
0.90K-0.10Na
Cell Type
b
Critical Current Density (mA/cm^2)
3
2
1
0
K
Na
Li
Hardness (MPa)
6
4
2
0
Li
Na
K
0
0.5
1
1.5
2
Equivalent Yield Stress (MPa)

Figure 6. Critical current density (CCD) vs electrochemical cell type and alkali metal yield stress. a) Average CCD value for each metal or alloy, including results across all areal capacities tested. Inset shows a simulation (see *Methods*) of the expected electrode microstructures for the semi-solid experiments, in which the liquid phase appears as white and solid crystalline phase particles as shades of gray. The vertical error bars in a) represent 95% confidence intervals for the critical current density according to the sample set. b) Critical current density versus equivalent yield stress (defined as hardness /3)[38] for solid Li, Na, and K metal in the present study. The vertical error bars in b) represent 95% confidence intervals for the critical current density according to the sample set. The horizontal error bars in b) represent the standard deviation of the measured values. The grey line serves as a guide for the eye. Inset figure: hardness for bulk Li, Na, and K metal. Each bar represents the average of 10 tests, with the error bar representing the standard deviation. These results indicate that the equivalent yield stress decreases in the order Li (at 1.74±0.1 MPa) to Na (at 0.41±0.08 MPa) to K (at 0.24±0.03 MPa).

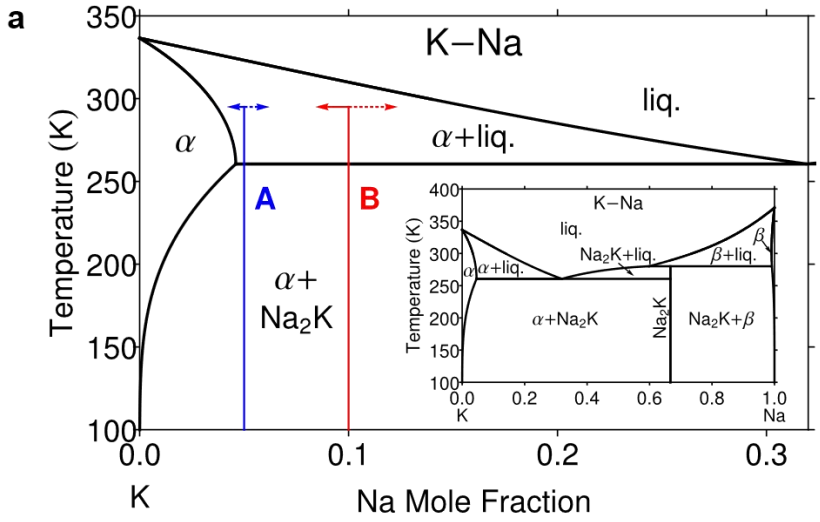
a
K–Na
liq.
α
α+liq.
A
B
α+
Na2K
Temperature (K)
Na Mole Fraction
K
Na2K+liq.
α+Na2K
Na2K+β
β+liq.

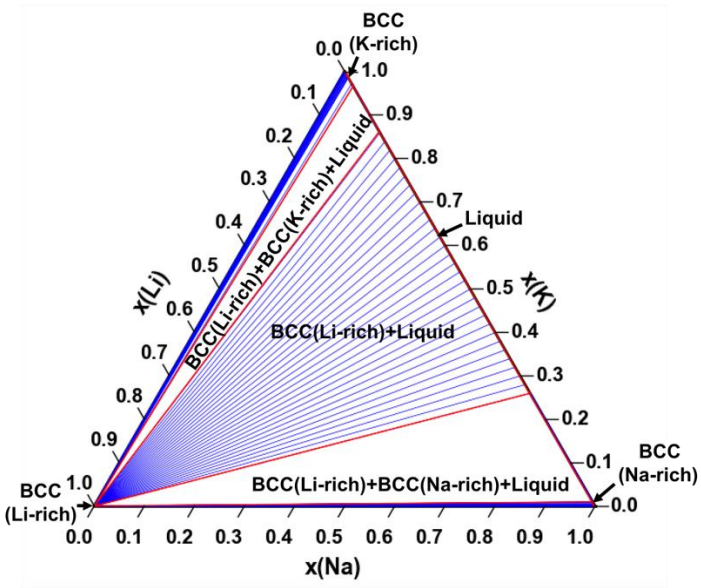
b
BCC
(K-rich)
BCC(Li-rich)+BCC(K-rich)+Liquid
Liquid
BCC(Li-rich)+Liquid
BCC(Li-rich)+BCC(Na-rich)+Liquid
BCC
(Li-rich)
BCC
(Na-rich)
x(Li)
x(K)
x(Na)

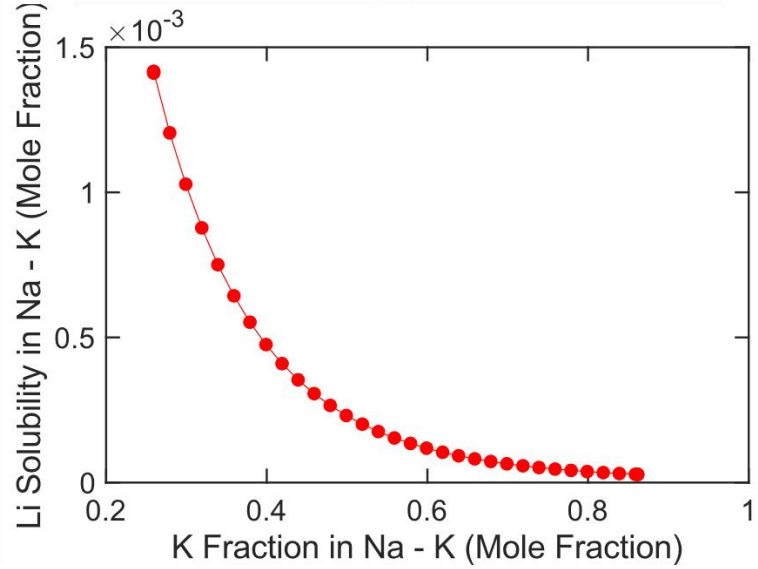
c
×10-3
Li Solubility in Na - K (Mole Fraction)
K Fraction in Na - K (Mole Fraction)

Figure 7. Compositional design for semi-solid alkali metal electrodes. a) Potassium-rich end of the computed Na-K binary phase diagram, with full phase diagram shown in the inset. Compositions A (0.95K-0.05Na) and B (0.90K-0.10Na) are shown by the vertical blue and red lines, respectively. The horizontal arrows pointing to the left and right show the composition change in each electrode of the present symmetric cell design upon cycling to 3 mAh·cm–2 areal capacity. For composition A, the calculated initial and terminal liquid phase percentages in the two electrodes of the symmetric cell are mol%, 3.8 mol% and 20 mol% respectively, while for composition B they are mol%, 38 mol% and 70 mol% respectively. b) Isothermal section of Li-Na-K at 300 K. The high mixing enthalpy between BCC Li and Na/K liquid leads to a low solubility of each in the other. A wide two-phase field exists within which nearly pure bcc Li co-exists with Na-K liquid (tie lines shown in blue). c) Solubility of Li in Na-K liquid decreases sharply with increasing K concentration of the liquid. The solid red curve serves as a guide for the eye.